Improved Transition and Reynolds Stress Modeling in RANS Simulations

René-Daniel Cécora[1], Rolf Radespiel[1], and Axel Probst[2]

[1] Technische Universität Braunschweig, Institute of Fluid Mechanics, D-38108, Braunschweig, Germany
r-d.cecora@tu-bs.de

[2] German Aerospace Center, Institute of Aerodynamics and Flow Technology, D-37073, Göttingen, Germany

Abstract. Recent developments in Reynolds-stress modeling for applications in aircraft aerodynamics are presented. These include a nonlinear pressure-strain correlation, sensitizing the length-scale equation to pressure gradients and large scale variations, laminar-turbulent transition modeling using linear stability analysis, and a careful calibration of model constants.

The improved Reynolds-stress model is used to simulate different subsonic and transonic airfoil flows as well as an oblique-shock/boundary-layer interaction, employing the unstructured flow solver DLR-TAU. Furthermore the simulation of the flow around an infinite swept wing is presented, in which the prediction and modeling of both Tollmien-Schlichting instabilities and cross-flow instabilities is included.

Keywords: CFD, turbulence modeling, second-moment closure, transition.

1 Introduction

The numerical simulation of relevant flows in aircraft aerodynamics requires statistical treatment of turbulence. An appropriate starting point are the Reynolds Averaged Navier-Stokes equations (RANS), which describe the time-averaged motion of fluid flow [1]. These equations consider turbulence as a Reynolds-stress tensor containing six different Reynolds stresses, which need to be provided by a turbulence model. Most of the turbulence models currently used by aircraft industry are based on the Boussinesq assumption (e.g. [2],[3]), which, as an analogue of the molecular viscosity, sets the Reynolds-stress tensor in relation to the mean strain rate tensor, with the scalar eddy viscosity μ_t as a constant of proportionality. Although these so-called eddy-viscosity models proved to yield reliable results for simple aerodynamic flows, they often fail in more complex flows including flow separation, streamline curvature or strong effects of stress anisotropy. In order to improve the performance of RANS modeling in more complex flows, Reynolds-stress turbulence models (RSM) are investigated.

Reynolds-stress models directly calculate transport equations for all elements of the Reynolds-stress tensor, hence the Boussinesq assumption is discarded.

N. Kroll et al. (eds.), *Computational Flight Testing*, Notes on Numerical Fluid Mechanics and Multidisciplinary Design 123,
DOI: 10.1007/978-3-642-38877-4_5,

Consequently turbulent stress anisotropy can be captured naturally, at the cost of higher computational effort. Beside the Reynolds-stress equations, RSM calculate an additional transport equation in order to evaluate the turbulent length scale, which is usually expressed by the dissipation rate ε or the specific dissipation rate ω. At the Institute of Fluid Mechanics of TU Braunschweig, a Reynolds-stress model by Jakirlić and Hanjalić [4] was implemented into the DLR flow solver TAU [5], which uses the homogeneous part of the dissipation rate as length scale variable [6]. Due to its advanced near-wall treatment of turbulence through calibrated damping functions and a wall-reflection pressure-strain model, the RSM can be considered as a so-called "low-Re" model, which has already shown its capabilities to simulate boundary layers in subsonic flows with pressure-gradients during the implementation process [6].

An undesirable side effect of the low-Re modeling is a delayed laminar-turbulent transition ([7],[8]), which can be evaded by locally providing a realistic Reynolds-stress distribution as a "transition tripping measure". Usually a simple generic distribution scaled with the local boundary-layer edge velocity gives a reliable transition behaviour. Physically more advanced is the determination of a realistic Reynolds-stress distribution from linear stability analysis, as described and implemented by Probst [8] for transition from Tollmien-Schlichting instabilities.

Within the framework of the research project *ComFliTe*, the physically advanced modeling of laminar-turbulent transition in combination with a Reynolds-stress model is extended to the consideration of cross-flow instabilities. The underlying theory as well as the application to the flow around an infinitive swept wing is presented in Sect. 3. Furthermore, different subsonic and transonic flows are simulated in order to check the industrial applicability of this turbulence model. An adjustment of coefficients in the length-scale equation of the model is necessary to achieve satisfying results, as can be seen in Sect. 4.

2 JHh-v1 / JHh-v2 Reynolds-Stress Model

Since Favre- and Reynolds-averaging of the Navier-Stokes equations produce a new unknown Reynolds-stress tensor, closure of the equation system with a turbulence model is required. Second-moment closure models use a transport equation for each of the six components of the Reynolds-stress tensor, which can be derived from the exact momentum equation, reading in general form [1]

$$\frac{\partial\left(\overline{\rho}\widetilde{R}_{ij}\right)}{\partial t}+\frac{\partial}{\partial x_k}\left(\overline{\rho}\widetilde{R}_{ij}\widetilde{U}_k\right)=\overline{\rho}P_{ij}+\overline{\rho}\Pi_{ij}-\overline{\rho}\varepsilon_{ij}+\overline{\rho}D^{\nu}_{ij}+\overline{\rho}D^{t}_{ij}+\overline{\rho}M_{ij}\ , \quad (1)$$

where only the production term P_{ij} and the viscous diffusion D^{ν}_{ij} can be calculated directly. However, all remaining terms on the right hand side of Eq. (1), which describe pressure-strain correlation, dissipation, turbulent diffusion as well as effects of compressibility, require modeling.

The JHh-v1 and JHh-v2 Reynolds-stress models are modified versions of the JHh model developed by Jakirlić and Hanjalić [4], which uses the homogeneous

dissipation rate ε^h as length scale variable in order to capture the correct dissipation rate profile close to walls. Probst [6] extended the length scale equation by two additional source terms, gaining promising results in different subsonic aerodynamic flows. This model version is now referred to as JHh-v1. For the application of the model to subsonic as well as transonic aerodynamic flows, an adaptation of coefficients in the length scale equation was conducted, furthermore a quadratic extension of the slow redistribution term [9] was added, resulting in the model version JHh-v2.

The JHh models employ a linear pressure-strain correlation with an additional wall-reflection model Π_{ij}^w according to Gibson and Launder [10], as well as the quadratic extension of the slow redistribution model mentioned above (term including C_1', only in JHh-v2):

$$\overline{\rho}\Pi_{ij} = \overline{\rho}\Pi_{ij,1} + \overline{\rho}\Pi_{ij,2} + \overline{\rho}\Pi_{ij}^w \tag{2}$$

$$\overline{\rho}\Pi_{ij,1} = -\varepsilon^h \overline{\rho}\left[C_1 \widetilde{a}_{ij} + C_1'\left(\widetilde{a}_{ik}\widetilde{a}_{jk} - \frac{1}{3}\delta_{ij}A_2\right)\right] \tag{3}$$

$$\overline{\rho}\Pi_{ij,2} = -C_2\overline{\rho}\left(P_{ij} - \frac{1}{3}P_{kk}\delta_{ij}\right) \ . \tag{4}$$

The model coefficients, including f_w, C_1^w and C_2^w within the wall-reflection model, contain near-wall damping functions which are calibrated based on DNS data [11]:

$$\begin{gathered} C_1 = C + \sqrt{A}E^2 \quad , \quad C_1' = -\max\left(0.7A_2; 0.5\right)C_1 \ , \\ C_2 = 0.8A^{1/2} \quad , \quad C = 2.5AF^{1/4}f \quad , \quad F = \min\left(0.6; A_2\right) \ , \\ f = \min\left[\left(\mathrm{Re}_t/150\right)^{3/2}; 1\right] \quad , \quad f_w = \min\left[\frac{\widetilde{k}^{3/2}}{2.5\varepsilon^h d}; 1.4\right] \ , \\ C_1^w = \max\left(1 - 0.7C; 0.3\right) \quad , \quad C_2^w = \max\left(A; 0.3\right) \ . \end{gathered} \tag{5}$$

These damping functions contain the turbulence Reynolds number $\mathrm{Re}_t = \widetilde{k}^2/(\nu\varepsilon^h)$, the turbulent kinetic energy $\widetilde{k}$, the local wall distance d as well as anisotropy invariants of the Reynolds-stress tensor (A, A_2) and of the homogeneous dissipation-rate tensor (E).

The anisotropic dissipation rate tensor ε_{ij} can be divided into a homogeneous part and a non-homogeneous part

$$\varepsilon_{ij} = \varepsilon_{ij}^h + \frac{1}{2}D_{ij}^\nu \ , \tag{6}$$

wherein the homogeneous part is approximated by an implicit relation:

$$\varepsilon_{ij}^h = f_s\widetilde{R}_{ij}\frac{\varepsilon^h}{\widetilde{k}} + (1 - f_s)\frac{2}{3}\delta_{ij}\varepsilon^h \quad \text{with} \quad f_s = 1 - \sqrt{A}E^2 \ . \tag{7}$$

The homogeneous dissipation rate ε^h is provided by a scalar length scale equation:

$$\frac{D\varepsilon^h}{Dt} = -C_{\varepsilon 1}\frac{\varepsilon^h}{\widetilde{k}}\widetilde{R}_{ij}\frac{\partial \widetilde{U}_i}{\partial x_j} - C_{\varepsilon 2} f_\varepsilon \frac{\varepsilon^h \tilde{\varepsilon}^h}{\widetilde{k}} + C_{\varepsilon 3}\nu\frac{\widetilde{k}}{\varepsilon^h}\widetilde{R}_{jk}\frac{\partial^2 \widetilde{U}_i}{\partial x_j \partial x_l}\frac{\partial^2 \widetilde{U}_i}{\partial x_k \partial x_l} + \frac{\partial}{\partial x_k}\left[\left(\frac{1}{2}\nu\delta_{kl} + C_\varepsilon \frac{\widetilde{k}}{\varepsilon^h}\widetilde{R}_{kl}\right)\frac{\partial \varepsilon^h}{\partial x_l}\right] + S_l + S_{\varepsilon 4} \tag{8}$$

with the low-Reynolds damping function

$$f_\varepsilon = 1 - \frac{C_{\varepsilon 2} - 1.4}{C_{\varepsilon 2}} \exp\left[-\left(\frac{\mathrm{Re}_t}{6}\right)^2\right] \quad . \tag{9}$$

Two additional source terms have been introduced into the length-scale equation, namely the length-scale limiter

$$S_l = \max\left\{\left[\left(\frac{1}{C_l}\frac{\partial l}{\partial x_n}\right)^2 - 1\right]\left(\frac{1}{C_l}\frac{\partial l}{\partial x_n}\right)^2; 0\right\}\frac{\varepsilon^h \tilde{\varepsilon}^h}{\widetilde{k}} A \quad \text{with} \quad l = \frac{\widetilde{k}^{3/2}}{\varepsilon} \tag{10}$$

and the pressure-gradient term

$$S_{\varepsilon 4} = -C^*_{\varepsilon 4}\frac{\varepsilon^h}{\widetilde{k}}\left(\widetilde{R}_{ss}\frac{\partial \widetilde{U}_s}{\partial x_s} + \widetilde{R}_{n_1 n_1}\frac{\partial \widetilde{U}_{n_1}}{\partial x_{n_1}} + \widetilde{R}_{n_2 n_2}\frac{\partial \widetilde{U}_{n_2}}{\partial x_{n_2}}\right) \quad , \tag{11}$$

to sensitize the equation to effects of non-equilibrium turbulence [6]. The source term $S_{\varepsilon 4}$ needs to be computed in streamline oriented coordinates (x_s, x_{n_1}, x_{n_2}). In order to ensure the applicability in a general flow solver, a transformation of the streamline oriented terms into the Cartesian coordinate system is required. This transformation can be found in [6]. The coefficients used in the length scale equation are provided in Table 1.

Table 1. Coefficients of the ε^h-equation

	$C_{\varepsilon 1}$	$C_{\varepsilon 2}$	$C_{\varepsilon 3}$	$C^*_{\varepsilon 4}$	C_ε	C_l
JHh-v1	1.44	1.80	0.30	1.16	0.18	2.5
JHh-v2	1.44	1.85	0.70	0.58	0.18	2.5

A generalized gradient diffusion model [12] is used for the components of the turbulent diffusion tensor, effects of compressibility are neglected.

3 Laminar-Turbulent Transition Modeling

In aeronautics, transition from laminar to turbulent flow is usually governed by the unstable growth of small-scale disturbances in the laminar boundary

layer. After a transitional phase of linear and non-linear amplifications, the 2D Tollmien-Schlichting (TS) or 3D cross-flow (CF) waves may reach a considerable amplitude before they finally break down into turbulence.

Within most RANS methods, the turbulent breakdown is considered as the transition point, which sharply distincts between laminar and turbulent regions. A common modeling approach is the so-called point transition, which deactivates or limits the turbulence-model production terms in the whole laminar regime. More complex transition models consider the effects of intermittency by introducing additional blending functions or transport equations. However, both the simple point-transition and the intermittency models usually neglect the above-mentioned fluctuations in the transitional region upstream of turbulence breakdown. Although these are not regarded as real turbulence, they formally produce Reynolds stresses in a statistical sense and may therefore contribute to a realistic modeling of turbulence onset within the RANS framework.

As demonstrated by Probst et al. [8], common RANS models using point transition fail to capture the strong onset of turbulence in laminar separation bubbles on low-Reynolds-number airfoils. For near-wall RANS models, such as the JHh-RSM considered here, transition to turbulence may even be fully suppressed, since the low-Reynolds damping terms interfere with the low freestream turbulence levels encountered in aeronautics.

In order to provide realistic contributions of the transitional fluctuations in Tollmien-Schlichting waves to the Reynolds stresses, [8] introduced a novel modeling concept based on linear stability theory (LST). These are inserted via turbulent source terms just ahead of the transition point, see Fig. 1, thus acting as a local "inflow condition" for the turbulent flow region. The derivation of the transitional input values applies a LST solver to compute the shapes of the Reynolds-stress profiles at the end of the linear amplification stage and scales them according to a DNS-based calibration.

Derived from the complex wave ansatz of 2D Tollmien-Schlichting waves, the Reynolds-stress shapes can be written as:

$$\overline{u_i u_j}^* = \frac{|\hat{u}_i| \cdot |\hat{u}_j|}{2} \cos\left(\varphi_{u_i} - \varphi_{u_j}\right) \quad . \tag{12}$$

Here, $|\hat{u}_i|$ are the amplitudes and φ_{u_i} the phase shifts of the most amplified wave f_0 (i.e. $N(f_0) = \max(N)$) at the end of the linear stage x_0. The amplitudes and phase shifts are obtained from the complex eigenfunctions of f_0 at x_0:

$$|\hat{u}_i| = \sqrt{\hat{u}_{i,R}^2 + \hat{u}_{i,I}^2} \quad , \qquad \varphi_{u_i} = \arctan \frac{\hat{u}_{i,I}}{\hat{u}_{i,R}} \quad , \tag{13}$$

whereas the position x_0 is computed via the classical e^N method.

In line with both numerical and experimental observations, the present modeling approach assumes that the (normalized) maximum streamwise velocity fluctuations $u'_{\max}/U_e$ (with U_e being the boundary-layer edge velocity) in a Tollmien-Schlichting wave reach a rather universal saturation amplitude before breakdown to turbulence occurs. The universal value of the normalized saturation level was obtained from DNS data of a transitional boundary layer in an

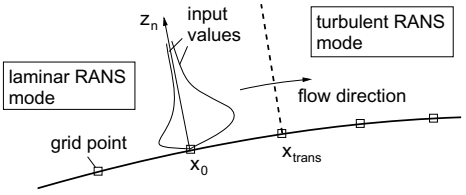

Fig. 1. Schematic illustration of the geometrical setup in the transitional region [8]

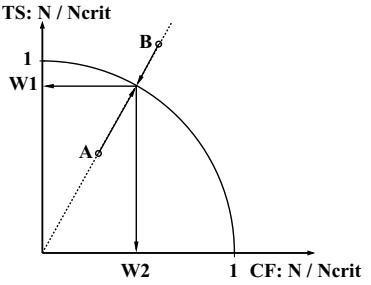

Fig. 2. Determination of weighting factors from N-factor-ratios

adverse pressure gradient and yield $|\hat{u}|_{\max}/U_e = 0.1$ or $\overline{u^2}_{\max}/U_e^2 = 0.005$, respectively. Thus, the required Reynolds-stress input values at x_0 can be determined from scaling the (normalized) Reynolds-stress shapes as:

$$\overline{u_i u_j}_0 = 0.005 \cdot U_e^2 \cdot \frac{\overline{u_i u_j}^*}{\overline{u^2}^*_{\max}} \quad . \tag{14}$$

Finally, the model is closed by computing the dissipation-rate input profile from the Reynolds-stress equations and the local amplification rate α_i.

This modeling concept for Tollmien-Schlichting transition was shown to greatly improve predictions of laminar separation bubbles on airfoils and yield consistent transition behaviour in flows as complex as stalling engine inlets [8]. The present work is aimed to extend the approach to 3D cross-flow instabilities, which are typically observed on swept wings.

In an equal way to the hitherto existing 2D approach, the most amplified cross-flow wave $f_{0,\mathrm{CF}}$ at position x_0 is determined. From its complex eigenfunctions, amplitude and phase shift are calculated via (13), leading to non-dimensionalized Reynolds-stress shapes (12). It can be expected that the amplitude of cross-flow waves reaches a saturation level which depends on the boundary-layer edge velocity as well. As a first estimation, the same factor $\overline{u^2}_{\max}/U_e^2 = 0.005$ is used for scaling the Reynolds-stress shapes resulting from cross-flow waves, therefore (14) is used for pure TS amplification as well as for pure CF validation. In cases of mixed amplification, contributions of Reynolds-stresses from both TS and CF waves have to be considered, applying weighting factors W_1 and W_2:

$$\overline{u_i u_j} = U_{e^2} \cdot \left(0.005 \cdot W_1 \cdot \left(\frac{\overline{u_i u_j}^*}{\overline{u^2}^*_{\max}} \right)_{\mathrm{TS}} + 0.005 \cdot W_2 \cdot \left(\frac{\overline{u_i u_j}^*}{\overline{u^2}^*_{\max}} \right)_{\mathrm{CF}} \right) \quad . \tag{15}$$

These weighting factors depend on the state of amplification in point x_0, more precisely on the relations $\left(\frac{N}{N_{\mathrm{crit}}}\right)_{\mathrm{TS}}$ and $\left(\frac{N}{N_{\mathrm{crit}}}\right)_{\mathrm{CF}}$. If the location at which transition is prescribed in the numerical simulation and the location at which transition is predicted by linear stability theory coincide, one of the weights

should be around 1 (assuming that no interaction between both types of instabilities is considered) and the other weight should be between 0 and 1. However, if the transition locations do not coincide, e.g. when limiting the movement of the transition line for stability reasons, unusual combinations of N-factor-ratios can appear. To prevent strong variations of the Reynolds-stress input values depending on the streamwise position, the weighting factors are determined from the unit circle in the $\left(\frac{N}{N_{\mathrm{crit}}}\right)_{\mathrm{TS}}$-$\left(\frac{N}{N_{\mathrm{crit}}}\right)_{\mathrm{CF}}$-map, as sketched in Fig. 2, reading:

$$W_1 = \left[1 + \frac{\left(\frac{N}{N_{\mathrm{crit}}}\right)^2_{\mathrm{CF}}}{\left(\frac{N}{N_{\mathrm{crit}}}\right)^2_{\mathrm{TS}}}\right]^{-1/2} \quad ; \quad W_2 = \left[1 + \frac{\left(\frac{N}{N_{\mathrm{crit}}}\right)^2_{\mathrm{TS}}}{\left(\frac{N}{N_{\mathrm{crit}}}\right)^2_{\mathrm{CF}}}\right]^{-1/2} \quad . \tag{16}$$

In order to validate the implementation of cross-flow transition modeling, a 2.5D infinite swept wing with ONERA-D airfoil in its cross section is simulated using the JHh-v2 model. The wing is swept at an angle of 60° and inclined to $\alpha = 4°$, flow conditions are $\mathrm{Re} = 2.39 \cdot 10^6$ and $\mathrm{M} = 0.23$. The 2-N-factors strategy of TAU transition module [13] is used to predict the transition locations on upper and lower surfaces. Critical N-factors are set to $N_{\mathrm{crit,TS}} = N_{\mathrm{crit,CF}} = 7.5$, furthermore no interaction between both instability types is considered.

The distribution of the pressure coefficient (Fig. 3a) shows that on the upper surface transition takes place in a laminar separation bubble. Stability analysis indicates that on the upper wing surface, mainly Tollmien-Schlichting instabilities are responsible for transition (Fig. 3b), while mixed amplification from Tollmien-Schlichting and cross-flow instabilities occurs on the lower surface (Fig. 3c). Experiments [14] show a transition location of $x_{\mathrm{tr}}/c = 0.35$ for the lower surface, indicating strong interaction between TS and CF instabilities. The predicted N-factors at this position are $N_{\mathrm{TS}} = 3.2$ and $N_{\mathrm{CF}} = 4$.

Fig. 4 shows the Reynolds-stress distributions that have been determined in the way described above for the lower surface of the airfoil. At first, the

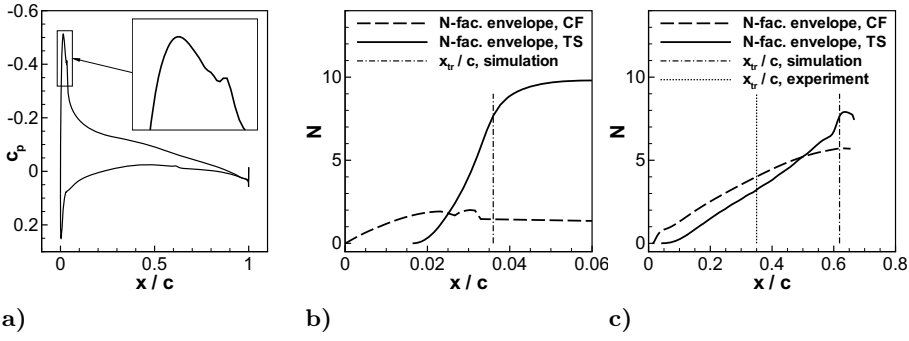

Fig. 3. 2.5D Swept Wing: a) pressure coefficient; b) N-factor envelope on upper surface; c) N-factor envelope on lower surface

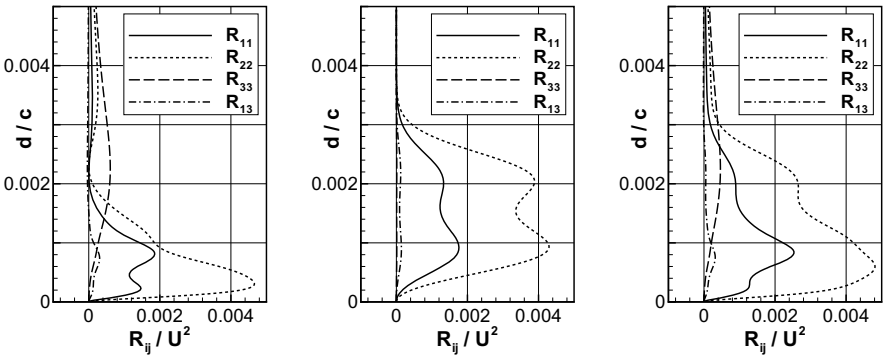

a) TS instabilities **b)** CF instabilities **c)** TS and CF instabilities

Fig. 4. 2.5D Swept Wing: prescribed Reynolds-stress distributions at transition location for lower surface

contributions of TS and CF instabilities are established individually (Fig. 4a and b), afterwards they are combined using (15) which can be seen in Fig. 4c).

4 Adjustment and Application of the Reynolds-Stress Model

All computations shown in this work have been carried out using the DLR-TAU Code [5], solving the RANS equations on hybrid unstructured grids with second order accuracy. As a reference, simulation results using the SST model by Menter [3] are also displayed.

4.1 Transonic Airfoil RAE 2822

The need to adapt coefficients in the length-scale equation becomes apparent when considering the flow around the RAE 2822 airfoil [15], which is a standard test case for turbulence models in transonic flow. Fig. 5 shows pressure distributions for two different flow conditions: Case 9 with Mach number $M = 0.73$ and Reynolds number $Re = 6.5 \cdot 10^6$ and Case 10 with Mach number $M = 0.75$ and Reynolds number $Re = 6.2 \cdot 10^6$, where in both cases the incidence is $\alpha = 2.8°$ and transition is prescribed at 3% chord on both sides.

In Case 9 as well as Case 10, the shock on the upper surface simulated by the JHh-v1 model is positioned clearly upstream of the experimental data.

Boundary-layer velocity profiles, shown in Fig. 6 directly downstream of the shock ($x/c = 0.65$) and further towards the trailing edge ($x/c = 0.90$), show that the JHh-v1 model overestimates the momentum loss of the boundary layer due to adverse pressure gradients. This leads to a reduced effective airfoil cambering in combination with an upstream movement of the shock.

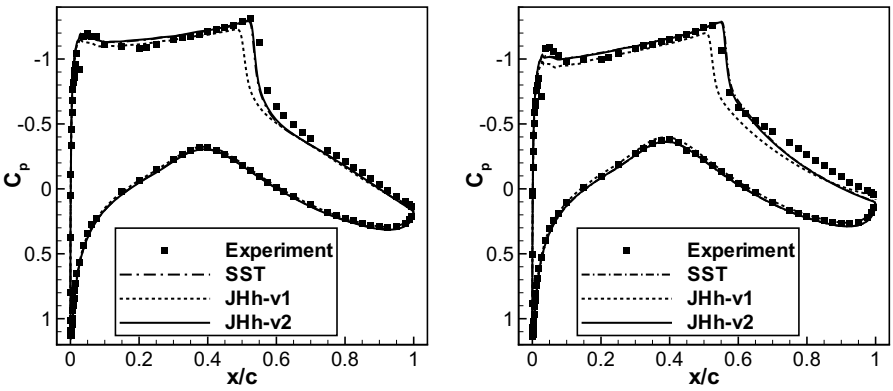

Fig. 5. RAE 2822 airfoil: pressure distributions for Case 9 (left) and Case 10 (right)

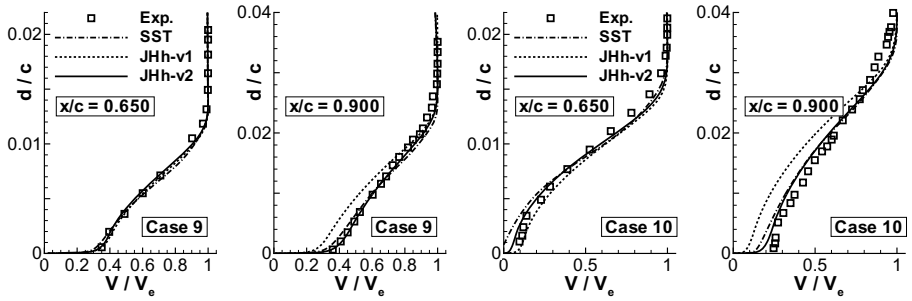

Fig. 6. RAE 2822 airfoil: velocity profiles in upper-surface boundary-layer

By reducing the coefficient of the pressure-gradient source term in the ε^h-equation (8), $C^*_{\varepsilon 4}$, the additional production of dissipation due to adverse pressure gradients is decreased, leading to higher levels of turbulence in the boundary layer and a smaller sensitivity towards adverse pressure gradients. This effect is amplified by increasing the coefficient of the sink term $C_{\varepsilon 2}$. As a result, the JHh-v2 model shows a closer accordance to the experimental data.

4.2 Subsonic Airfoil HGR-01

The reduced sensitivity towards adverse pressure gradients has an influence on the performance in subsonic high-lift flows as well, which can be seen for the horizontal stabilizer airfoil HGR-01 at Mach number M = 0.073 and Reynolds number Re = 656500. The agreement to experiments of the lift coefficient at high angles of attack is slightly decreased (Fig. 7), the maximum lift coefficient is now overestimated by 8.5%. The higher lift coefficient results from a smaller momentum loss in the boundary layer and a smaller trailing edge separation, as indicated in Fig. 8. Nonetheless improvements compared to the SST model can be seen.

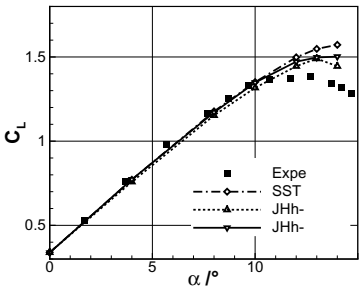

Fig. 7. HGR-01 airfoil: lift curve, M = 0.073, Re = 656500

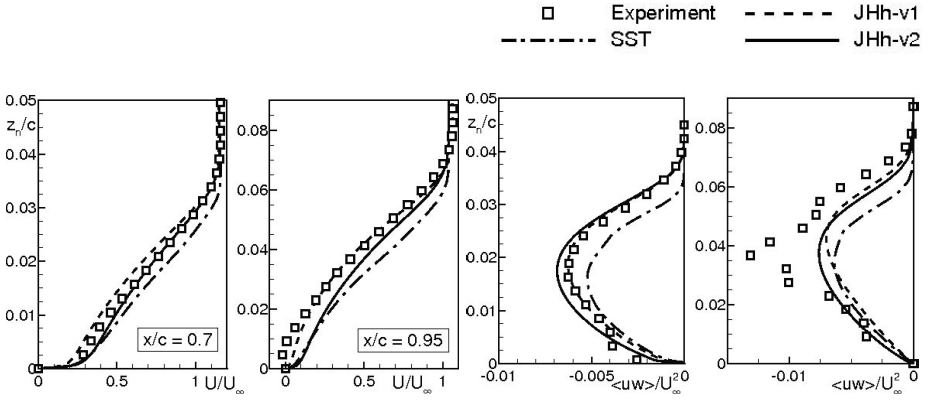

Fig. 8. HGR-01 airfoil: velocity and turbulent shear stress profiles near trailing edge

4.3 Zero Pressure-Gradient Flat Plate

Increasing the coefficient $C_{\varepsilon 2}$ reduces the dissipation rate, which involves a higher skin friction in the boundary layer of a flat plate without pressure gradient. By simultaneously increasing the coefficient $C_{\varepsilon 3}$, the skin friction can be reduced to reasonable values. Since the JHh-v1 model simulates higher levels of skin friction compared to available experimental data, $C_{\varepsilon 3}$ was increased beyond the point of compensating the skin friction influence of $C_{\varepsilon 2}$. The resulting skin friction coefficient for a zero pressure-gradient flat plate is shown in Fig. 9.

4.4 Oblique-Shock/Boundary-Layer Interaction

The behaviour of the Reynolds-stress models in shock-induced separation can be examined when simulating the interaction of an oblique shock with a flat-plate boundary-layer. Numerous experiments have been carried out at the Institut Universitaire des Systèmes Thermiques Industriels (IUSTI), Marseille, France, using a supersonic wind tunnel at Mach 2.3 [16], [17], [18]. The shock, created by

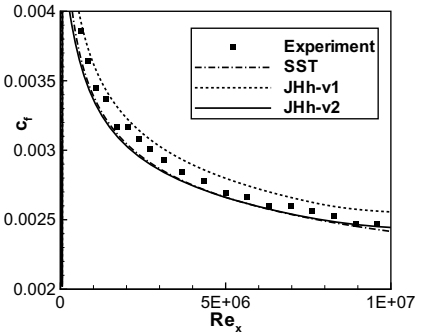

Fig. 9. Skin-friction coefficient along Zero Pressure-Gradient Flat Plate, M = 0.1

a sharp-edged plate which is placed with an angle of 8 degrees into the freestream, is strong enough to force separation of the turbulent boundary layer.

The size of the shock-induced separation shows a high sensitivity towards the thickness of the incoming boundary layer, which was adapted by varying the length of the computational domain upstream of the interaction region. Both for experiments and numerical simulations, the boundary layer thickness and skin friction coefficient of the boundary layer upstream of the interaction region are listed in Table 2.

The shock-wave/boundary-layer interaction region, simulated with the JHh-v2 model, can be seen in Fig. 10a. The surface pressure distribution in Fig. 10b indicates an earlier pressure rise when using the JHh-v1 model compared to the other turbulence models. This is due to bigger extensions of the separation bubble, both in streamwise and in normal direction, and a higher momentum loss of the boundary layer.

These observations can be made when comparing velocity profiles in the boundary layer (Fig. 11). While the JHh-v1 model clearly overestimates the influence of the shock on the boundary layer, the JHh-v2 model shows better agreement to the experimental data. Figure 11 furthermore includes profiles of the square root of the Reynolds-stress components $\widetilde{R}_{11}$ and $\widetilde{R}_{33}$, respectively, simulated with the Reynolds-stress models as well as the SST model in comparison to PIV data. Here the improved modeling of turbulent stresses within the differential Reynolds-stress models, especially their capability of accounting for Reynolds-stress anisotropy, is clearly visible. The JHh-v1 and JHh-v2 models predict higher levels of streamwise Reynolds stress than wall-normal Reynolds

Table 2. Boundary layer upstream of the interaction region, $X = 260$ mm

	experiments	JHh-v1	JHh-v2	Menter SST
δ_0(mm)	11	10.98	10.97	10.94
c_f	0.002	0.00214	0.00200	0.00202

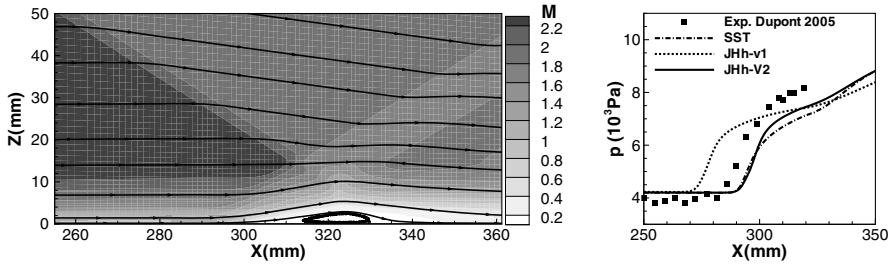

a) b)

Fig. 10. Oblique-Shock/Boundary-Layer Interaction: a) flow field and b) surface pressure distribution

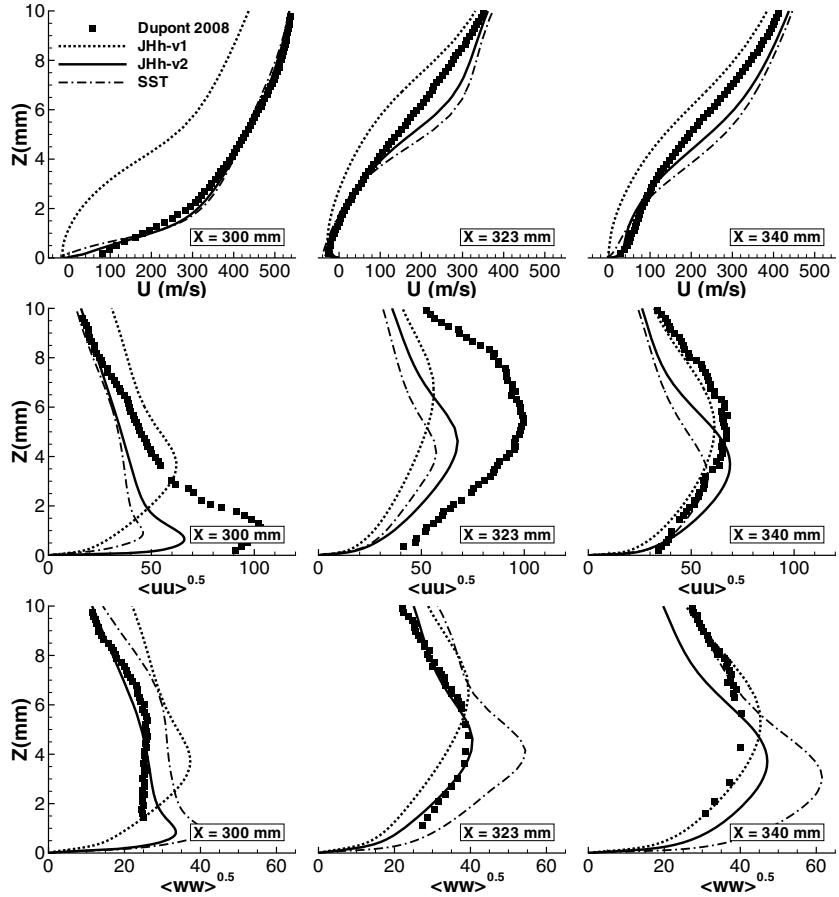

Fig. 11. Oblique-Shock/Boundary-Layer Interaction: velocity and turbulence profiles

stress, which is confirmed by the experiment. As a result of its inherent assumption of stress isotropy, the SST model is unable to capture these differences.

4.5 Laminar Airfoil NLF9

For simulating the flow around the laminar airfoil NLF9, the TAU transition module has been used in combination with the earlier discussed turbulence models. The advanced transition modeling (Sect. 3) was applied to determine Reynolds stresses directly upstream of the transition point, as a matter of the simplification to a 2D flow only considering Tollmien-Schlichting instabilities. All simulations have been performed on a 2D hybrid grid, containing 78000 points. Measurements of the surface pressure were conducted in the cryogenic Ludwieg tube (KRG) in Göttingen, furthermore the heat flux was measured to give an indication of the transition location. The upper part of Fig. 12 shows the comparison of experimentally and numerically achieved surface pressure distributions, for subsonic free stream conditions (Case 68: $\mathrm{M} = 0.30$, $\mathrm{Re} = 6 \cdot 10^6$, $\alpha = 5°$) as well as for transonic free stream conditions (Case 95: $\mathrm{M} = 0.62$, $\mathrm{Re} = 15 \cdot 10^6$, $\alpha = 3°$). To compensate for effects of the wind tunnel side walls, the angle of attack was reduced in the simulations until the measured lift coefficient was reached, as listed in the Tables 3 and 4. It is noticable that both turbulence models show almost similar pressure distributions for both test cases, with a good agreement to the experimental data.

Table 3. NLF 9 airfoil, Case 68: experimental and numerical flow properties

	C_L	α	$(x_\mathrm{tr}/c)_\mathrm{upper}$	$(x_\mathrm{tr}/c)_\mathrm{lower}$
experiments	0.9213	5°	0.15 − 0.25	0.55 − 0.65
SST	0.9253	3.55°	0.130	0.573
JHh-v2	0.9211	3.53°	0.114	0.564

Table 4. NLF 9 airfoil, Case 95: experimental and numerical flow properties

	C_L	α	$(x_\mathrm{tr}/c)_\mathrm{upper}$	$(x_\mathrm{tr}/c)_\mathrm{lower}$
experiments	0.9116	3°	0.45 − 0.50	0.55 − 0.60
SST	0.9207	1.4°	0.470	0.534
JHh-v2	0.9145	1.4°	0.468	0.534

Since skin friction rises drastically after transition to a turbulent boundary layer, the total value of heat flux between surface and fluid rises likewise. This behaviour can be seen in the bottom part of Fig. 12. At the lower Mach number $\mathrm{M} = 0.30$, the heat flux for a turbulent surface seems to be at least $-1\mathrm{K/s}$, consequently the experimental transition location for Case 68 can be estimated to $x/c = 0.15...0.25$ (upper surface) and $x/c = 0.55...0.65$ (lower surface). Developing a more distinct jump in heat flux at the higher Mach number $\mathrm{M} = 0.62$, the

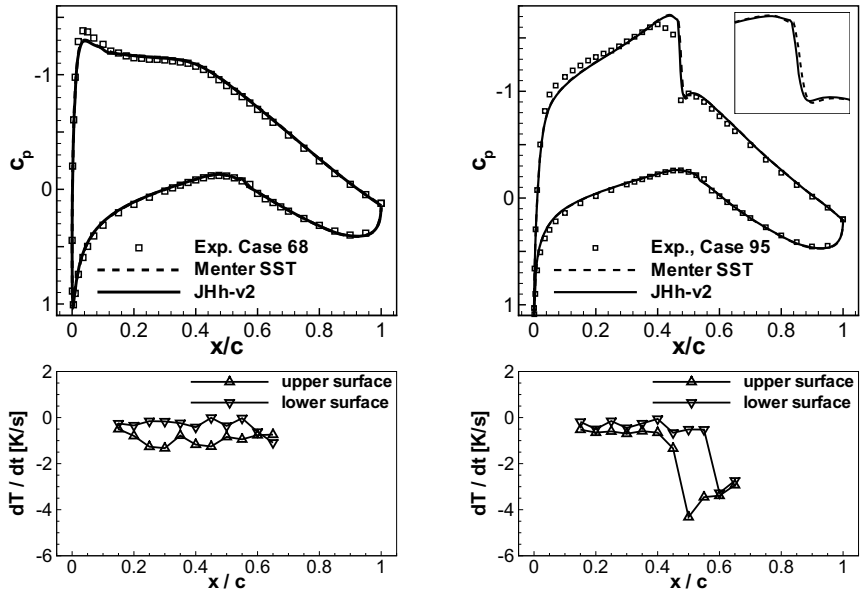

Fig. 12. NLF 9 airfoil: pressure distributions (top) and heat flux (bottom) for Case 68 (left) and Case 95 (right)

experimental transition location for Case 95 can be estimated to $x/c = 0.45...0.50$ (upper surface) and $x/c = 0.55...0.60$ (lower surface). The transition locations predicted by the TAU transition module are listed in the Tables 3 and 4, showing good agreement to the experimental values as well.

5 Conclusion

Improvements of the Low-Re JHh Reynolds-stress turbulence model have successfully been implemented and tested in different applications of aircraft aerodynamics using the DLR-TAU code.

By considering linear stability analysis, the RSM allows for a physically advanced modeling of laminar-turbulent transition. Using eigenfunctions of instabilities in the laminar boundary layer, local Reynolds stresses can be derived and prescribed at the transition point. This approach, before only applicable to Tollmien-Schlichting instabilities, has been extended to cross-flow instabilities and tested with the simulation of an infinite swept wing flow.

Furthermore an adjustment of coefficients in the length-scale equation of the Reynolds-stress model was undertaken, by which the performance of the

model could be improved for transonic airfoil flows as well as for an oblique-shock/boundary-layer interaction flow.

Acknowledgments. The authors gratefully acknowledge the "Bundesministerium für Bildung und Forschung" who funded this research within the frame of the joint project *ComFliTe* (funding number 20 A 06 04 G).

Also we would like to thank N. Krimmelbein of DLR for providing simulation meshes of the *infinite swept wing* test case.

References

1. Wilcox, D.C.: Turbulence Modeling for CFD, 2nd edn. DCW Industries, La Cañada, CA (1998)
2. Spalart, P.R., Allmaras, S.R.: A one-equation turbulence model for aerodynamic flows. La Recherche Aèrospatiale 1, 5–21 (1994)
3. Menter, F.R.: Two-Equation Eddy-Viscosity Turbulence Models for Engineering Applications. AIAA Journal 32(8), 1598–1605 (1994)
4. Jakirlić, S., Hanjalić, K.: A new approach to modelling near-wall turbulence energy and stress dissipation. Journal of Fluid Mechanics 459, 139–166 (2002)
5. Kroll, N., Rossow, C.-C., Schwamborn, D.: The MEGAFLOW-Project - Numerical Flow Simulation for Aircraft. In: Progress in Industrial Mathematics at ECMI 2004. Springer, Heidelberg (2005)
6. Probst, A., Radespiel, R.: Implementation and Extension of a Near-Wall Reynolds-Stress Model for Application to Aerodynamic Flows on Unstructured Meshes. AIAA Paper 2008-770 (2008)
7. Rumsey, C.L., Pettersson Reif, B.A., Gatski, T.B.: Arbitrary Steady-State Solutions with the K-Epsilon Model. AIAA Journal 44(7), 1586–1592 (2006)
8. Probst, A., Radespiel, R., Rist, U.: Linear-Stability-Based Transition Modeling for Aerodynamic Flow Simulations with a Near-Wall Reynolds-Stress Model. AIAA Journal 50(2), 416–428 (2012)
9. Lumley, J.L.: Computational Modeling of Turbulent Flows. Adv. Appl. Mech. 18, 123–176 (1978)
10. Gibson, M.M., Launder, B.E.: Ground Effects on Pressure Fluctuations in the Atmospheric Boundary Layer. Journal of Fluid Mechanics 86, 491–511 (1978)
11. Jakirlić, S., Hanjalić, K.: A Second-Moment Closure for Non-Equilibrium and Separating High- and Low-Re-Number Flows. In: Proc. 10th Symposium on Turbulent Shear Flows, The Pennsylvania University, USA, August 14-16 (1995)
12. Daly, B.J., Harlow, F.H.: Transport equations of turbulence. Physics of Fluids 13, 2634–2649 (1970)
13. Krimmelbein, N., Radespiel, R.: Transition prediction for three-dimensional flows using parallel computation. Computers & Fluids 38(1), 121–136 (2009)
14. Arnal, D., Juillen, J. C.: Three-dimensional transition studies at ONERA/CERT. AIAA Paper 87-1335 (1987)
15. Cook, P.H., McDonald, M.A., Firmin, M.C.P.: Aerofoil RAE 2822 – Pressure Distributions, and Boundary Layer and Wake Measurements. In: Barche, J. (ed.) Experimental Data Base for Computer Program Assessment, AGARD-AR-138, Chapter A6 (1979)

16. Delery, J., Marvin, J.G.: Shock Wave-Boundary Layer Interactions. NATO, AGARDograph No. 280 (1986)
17. Dupont, P., Haddad, C., Ardissone, J.P., Debiève, J.F.: Space and time organisation of a shock/turbulent boundary layer interaction. Aerospace Science and Technology 9, 561–572 (2005)
18. Dupont, P., Piponniau, S., Sidorenko, A., Debiève, J.F.: Investigation by Particle Image Velocimetry Measurements of Oblique Shock Reflection with Separation. AIAA Journal 46(6) (2008)